

Communication

Sensing Performance Analysis of Spiral Metasurface Utilizing Phase Spectra Measurement Technique

Oleg Kameshkov ^{1,2} , Vasily Gerasimov ^{1,2,*}  and Sergei Kuznetsov ^{2,3}¹ Budker Institute of Nuclear Physics SB RAS, 630090 Novosibirsk, Russia² Physics Department, Novosibirsk State University, 630090 Novosibirsk, Russia³ Rzhanov Institute of Semiconductor Physics SB RAS, Novosibirsk Branch "TDIAM", 630090 Novosibirsk, Russia

* Correspondence: v.v.gerasimov3@gmail.com

Abstract: We have demonstrated both numerically and experimentally a 2D plasmonic metamaterial the unit cell of which comprised an Archimedean spiral with a C-shaped resonator. Such metasurface enables the excitation of spoof localized plasmon resonances (LPRs) in the terahertz frequency range, similar in properties to the familiar LPRs in the visible range. We have compared the thin-film sensing potentials of the fundamental and dark resonant modes supported by the metasurface in the range of 0.2–0.5 THz. Both the amplitude and phase transmission spectra have been studied. A sensitivity of 21.1%/RIU (78.7 GHz/RIU) and a figure of merit (FOM) of 14.4 RIU⁻¹ have been achieved. The FOM and Q factor obtained from the phase transmission spectra were shown to be about twice higher than those obtained from the amplitude spectra.

Keywords: terahertz sensors; spiral 2D metamaterial; phase spectrum; spoof localized surface plasmon resonance



Citation: Kameshkov, O.; Gerasimov, V.; Kuznetsov, S. Sensing Performance Analysis of Spiral Metasurface Utilizing Phase Spectra Measurement Technique. *Photonics* **2023**, *10*, 243. <https://doi.org/10.3390/photonics10030243>

Received: 28 December 2022

Revised: 14 February 2023

Accepted: 21 February 2023

Published: 23 February 2023



Copyright: © 2023 by the authors. Licensee MDPI, Basel, Switzerland. This article is an open access article distributed under the terms and conditions of the Creative Commons Attribution (CC BY) license (<https://creativecommons.org/licenses/by/4.0/>).

1. Introduction

Plasmonics is the area of photonics based on the coupling of electromagnetic waves with free electrons and polaritons in metals or semiconductors. There are two main types of plasmon excitation in metals, which yield surface plasmons (SPs) and localized surface plasmons (LSPs). The known SPs are electron waves propagating along a metal-dielectric interface, whereas LSPs are localized electron oscillations in metal nanoparticles [1]. Because of the remarkable ability to confine light on a metal surface within a subwavelength region, SPs and LSPs have various applications, such as ultra-high-resolution imaging [2], nanoplasmonic waveguides [3], improved light collection in solar cells [4], and luminescence amplification [5]. These properties and phenomena are associated with the dielectric permittivity of metals. Negative dielectric permittivity leads to the emergence of an evanescent wave on the metal-dielectric interface, penetrating both the metal medium and the dielectric one. However, highly localized and confined SPs exist only in the visible and infrared ranges. In the low-frequency range, metals behave like almost perfect electric conductors and as consequence, only a small part of the electric field penetrates the metal. It leads to weak confinement of plasmons by the surface of the metal and rapid destruction of this state [6].

Metamaterials are artificial materials typically consisting of the periodically placed subwavelength unit cell ('meta-atoms'). These unit cells are built from dielectric or metallic materials, but their exact shape and geometry can drastically affect the interaction of light with them. The use of metamaterials significantly expanded the potential capabilities of current photonic materials and devices in controlling electromagnetic waves. Based on the metamaterial approach, scientists realized exciting concepts such as negative refraction [7] and cloaking [8,9]. In addition to these well-known concepts, in 2004, Pendry et al. suggested a new metamaterial approach, which enabled the demonstration of the

excitation of surface waves on a metal surface structured by tiny holes [10]. Comparing the dispersion curves and mode profiles, they found that electromagnetic waves propagating along such surfaces in the spectrum from microwave to far-infrared are close analogs of the familiar SPs at optical frequencies. As a consequence, these waves were called ‘spoof’ surface plasmons [11]. Another way to generate SSPs is using a 1D periodic grating with a period less than half of the wavelength of the incident wave. In this case, such a structure can be considered as a metamaterial or an effective medium with a dielectric permittivity of the Drude type, depending on the parameters of the grating [12]. Subwavelength gratings supporting spoof plasmons are valuable for sensing applications. For instance, Ng Binghao et al. were the first who experimentally demonstrated the measurement of the refractive index of nitrogen and various liquids with such gratings, using time-domain spectroscopy in 2013 [13]. Yi Huang et al. realized ultraprecision THz SSPR sensors with direct phase readout capacity [14]. The last article in which Yao H. et al. raised the question of spectral analysis of molecules with subwavelength grating-based sensors was published in 2022 [15].

However, the bulkiness and low efficiency of SSP devices limited their opportunities until Shen et al. [16] developed and investigated ultrathin periodic metal strips similar to compressed 1D gratings with near-zero thickness. Conformal surface plasmons propagating on them have opened the route to new flexible miniature tools [11]. Further investigations showed that a spoof plasmon polariton concept also enabled the imitation of features of localized surface plasmon polaritons in the low-frequency range. A subwavelength grating compressed and rolled into a closed surface can be described as a 2D topologically closed flat metamaterial (or metasurface), which supports spoof localized SPs. The first metamaterial of this type was demonstrated by Pors in 2012 [17]. This work was followed by a large number of studies devoted to periodically textured cylinders and the improvement of their resonance and excitation performances [11,18,19]. In particular, it was shown that aside from fundamental modes imitating the familiar localized plasmons, a C-shaped resonator placed in the vicinity of a textured cylinder can excite dark modes. These dark modes had higher quality factors [20]. Lately, only two works related to sensing were published, which demonstrated that an LSSP metamaterial can be used as a microfluidic sensor in the microwave and terahertz frequency ranges [21,22].

Although spoof localized resonance modes have been observed on periodically textured cylinders, they are not subwavelength in the lateral directions because their lowest resonance frequency of them is limited by their size. This can be overcome via either integration of the high-index materials of the substrate with such metamaterials, which is too difficult, or the usage of spiral grooves. The longer the spiral, the longer the SPR resonance wavelength, and as a consequence, it exceeds the size of the structure, which leads to stronger electromagnetic field localization near the surface. The first work devoted to spiral metallic metamaterials was published in 2014. Huidobro with his colleagues supposed and demonstrated experimentally that magnetic SLSPRs can be excited on such metastructures [23]. A year later, a group of scientists combined a spiral metamaterial with a corrugated metallic strip, which enabled the coupling of spoof SPs to spoof LSPs at microwave frequencies [24]. In 2016, Gao Z. et al. investigated stereo metamaterials based on a stack of metallic spiral structures and found strong magnetic coupling effects [25]. Then Gao Z. with other colleagues showed that a complementary metallic spiral structure supports higher-order spoof-LSPs [26]. In the same year, two articles were written by Liao Z. et al. [27,28]. In the first one, the authors described an analytical model of localized spoof plasmons in spiral geometries within the framework of the effective medium theory, whereas, in the second work, the researchers showed that ultrathin metallic spirals support both electric and magnetic localized spoof plasmons in the terahertz frequency range. In addition, the electromagnetically induced transparency effect was demonstrated. Zhang J. et al. studied the interaction of two closely spaced spiral meta-atoms and the excitation of hybrid plasmon modes enhancing electric fields in 2017 [29]. After that, Huang Y. et al. replaced symmetrical spiral metamaterials with nonconcentric structures and considered

their influence on mode hybridization and field enhancement within nanogaps [30]. In 2018, Hai Su et al. suggested another application of these metamaterials [31]. They excited deep-subwavelength near-field electromagnetic spoof plasmons with an orbital angular momentum. In the ensuing year, scientists generated enhanced magnetic localized spoof plasmons using two vertical conductively-connected metallic spiral structures [32]. Another group of researchers studied different configurations of spiral metamaterials for the sensing application of thin films in the terahertz frequency range [33].

To sum up, it was shown that THz spoof LSPs have several advantages over the familiar LSPs in the visible range for creating high-performance sensors. SLSRs depend on the geometry of the meta-particle, which provides flexibility in designing the electromagnetic properties of structures. Spoof LSP metasurfaces can provide high field confinement, and large field enhancement in the vicinity of the surface. Moreover, the ohmic losses, which limit the sensitivity of sensors in the visible range, can be neglected at low frequencies. As a result, the Q-factor of resonances and their figure of merits achievable in the THz frequency range are comparable or higher than that in the optical range, and it is possible to realize sensors for solving the problems of investigations of thin layers [34], as well as spectroscopy of tiny biological objects at the terahertz frequencies [35]. Refractive index sensing or spectroscopy in the THz region is of great interest for biological and medical applications because many absorption spectral lines of complex molecules lie in the THz range.

In this paper, we examine, both numerically and experimentally, the sensing capabilities of various resonant modes supported by metamaterials comprising Archimedean spirals with C-shaped resonators in the THz range. For our study, we have used a loss-less analyte of different thicknesses, coating the metamaterial. We compared the sensitivity, Q factor, and figure of merit (FOM) obtained from the amplitude and phase transmission spectra. The paper is organized as follows. First, we discuss physical phenomena that lie in the excitation of modes on such metamaterial and the reasons for choosing metamaterial parameters. Second, we introduce numerical and experimental schemes for obtaining transmission spectra. Next, the features of the fabrication of metamaterials by means of the conventional lithographic process are described. Finally, we compare and analyze the sensor characteristics of the proposed metamaterial. The results are summarized in the concluding section. Our research made it possible to improve the resonance performance of the high-sensitivity THz sensor, allowing measuring the refractive index and thickness of different substances.

2. Design of Spiral Metasurface

A design of an Archimedean-spiral metamaterial with a C-shaped resonator is demonstrated in Figure 1a. The spiral structure can be described with the following parametric equations [36]:

$$\begin{aligned} x(\theta) &= \left(r_{in} + \frac{(R-r_{in})\cdot\theta}{2\pi m} \right) \cos(\theta) \\ y(\theta) &= \left(r_{in} + \frac{(R-r_{in})\cdot\theta}{2\pi m} \right) \sin(\theta) \end{aligned} \tag{1}$$

where R is the radius of the spiral, r_{in} is the distance of the starting point from the origin (it was $r_{in} = 0$ in our case), m is the number of arms, and θ is the angle of the spiral in the range from $\theta_{in} = 0$ to $\theta_{fin} = 2\pi m$.

Spoof localized plasmons excited on such structures are standing waves on a loop. With an increase in the length of the loop, the resonance shifts to a lower frequency, which makes the structure deeply subwavelength with high confinement of the LSPR modes near the surface. On the other hand, since the Archimedean spiral structure is a compressed and rolled subwavelength grating, the asymptotic frequency corresponding to the maximum operating frequency can be estimated as [18]

$$f_a \sim \frac{c}{4h \cdot n_s} = \frac{c \cdot \pi \cdot m}{n_s \cdot R \cdot \left[\theta_{fin} \sqrt{1 + \theta_{fin}^2} + \ln \left(\theta_{fin} + \sqrt{1 + \theta_{fin}^2} \right) \right]} \tag{2}$$

where h is the length of the arm and n_s is the refractive index of the substrate, and c is the speed of light. We used thin polypropylene (PP) with dielectric permittivity $\epsilon_s = n_s^2 = 2.25 \cdot (1 - i \cdot 10^{-3})$ [37,38] as a substrate, which allowed us to minimize the dielectric losses and diminish the interference effects in the PP layer. The number of arms and their width w are limited by the radius of the structure and fabrication process. m influences the number of high-order modes that can be excited, nonlocal effects, and stability against the angle of incidence [27,29]. In our case, these parameters were $m = 12$ and $w = 8 \mu\text{m}$. Based on previous investigations [33], we have chosen the structure radius $R = 192 \mu\text{m}$. Thus, using Equation (2), we can calculate the asymptotic frequency $f_a \approx 0.9 \text{ THz}$, and this frequency lies on the upper side of the operating frequency range of our terahertz source.

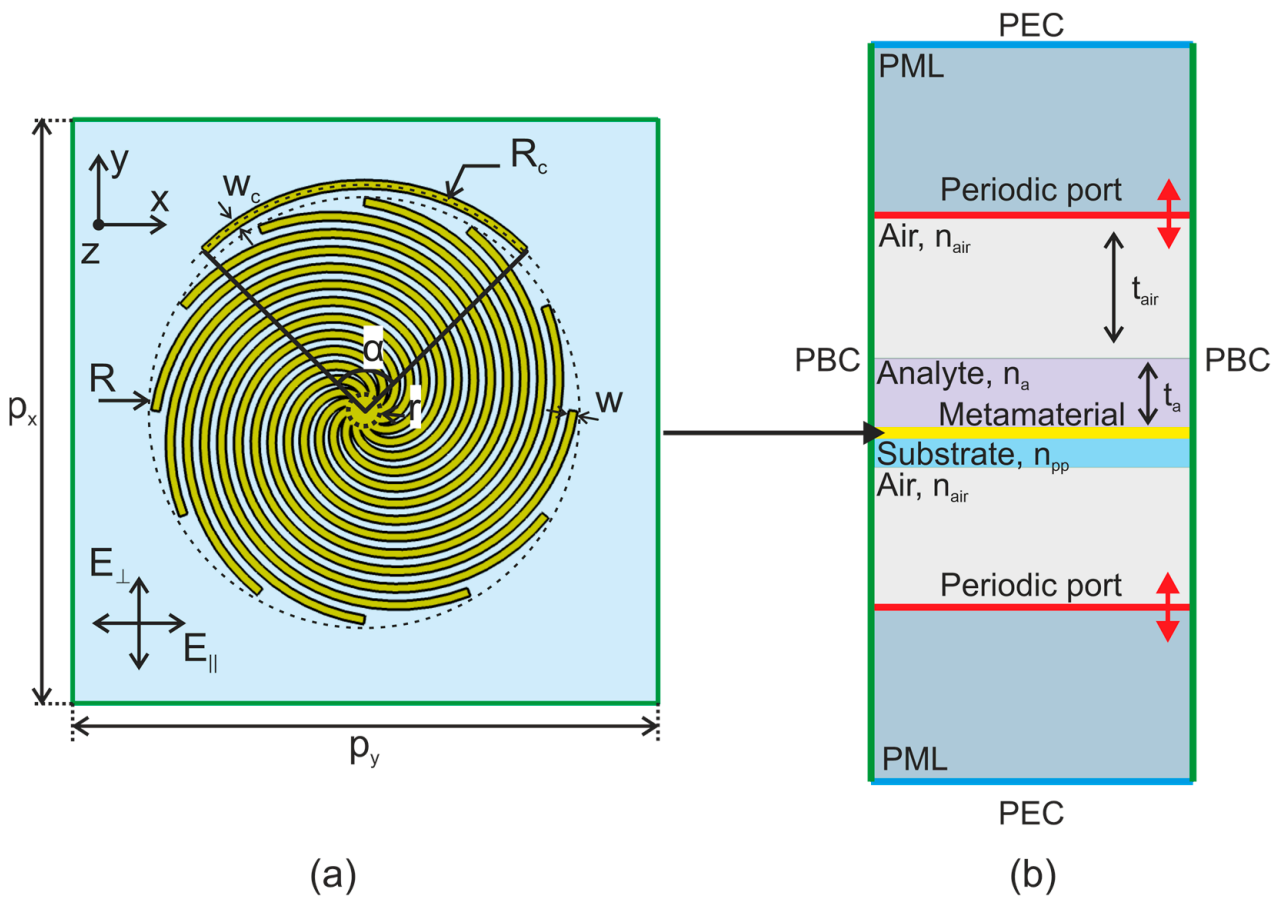


Figure 1. (a) Schematic representation of spiral metamaterial. (b) Numerical scheme for modeling with COMSOL.

Another parameter of the metamaterial is the lateral periodicity of spiral structures in the x - and y - directions (p_x and p_y , correspondingly). It affects the interaction of fields from adjacent structures (hybridization effect) and the emergence of diffraction modes. The position of diffraction modes can be calculated with [39]

$$\lambda_s = \frac{pn_d \cdot (1 - \sin \beta)}{s} \quad (3)$$

where s is the diffraction order, n_d is the refractive index of the surrounding media, and β is the incident angle. The period of the structure $p_x = p_y = 768 \mu\text{m}$ was chosen so that the diffraction dip was far from other metamaterial resonances and the hybridization effect was negligible.

The spiral metamaterial supports a low Q factor fundamental dipole ‘bright’ mode and high Q factor ‘dark’ modes. To excite a fundamental mode, it is sufficient to illuminate the

structure with a plane wave under normal incidence, while dark modes can be excited by means of grazing incidence, C-shaped dipole resonator, spoof LSP resonator, or near-field coupling [20]. In this work, we used a C-shaped dipole resonator to produce the dark modes with far-field excitations at normal incidence. The principle is that, after excitation of the auxiliary resonator by a plane wave, dark modes are excited by the evanescent coupling. Since dark modes are more sensitive and have a higher figure of merit than the fundamental mode, they are more promising for sensor applications. The C-shaped resonator was placed as close as possible to the spiral structure to increase the efficiency of the excitation, and the distance to the central part of the resonator $R_C = 204 \mu\text{m}$ and its width $w_C = 8 \mu\text{m}$ were limited by the fabrication process. According to [33], the resonator arc angle α was chosen to be 90° .

3. Numerical Scheme

To predict the resonance characteristics of spiral sensors we used the COMSOL Multiphysics software, which enabled the calculation of the metasurfaces by the finite element method. The 2D metamaterial was simulated in the 3D space. An elementary Floquet cell consisted of a metal Archimedean spiral with a C-shaped resonator. It was limited by periodic boundary conditions on its four sides for the calculation of an infinite 2D array as shown in Figure 1b. The Al metal layer was modeled as a transition boundary condition with the electrical conductivity $\sigma = 1.5 \cdot 10^7 \text{ S/m}$ [37,38] and thickness $t_m = 0.35 \mu\text{m}$. A thin layer of analyte was calculated as a conventional domain, but a structured mesh was used for modeling it.

Perfectly matched layers (PMLs) were applied to the lowest and highest parts of the Floquet cell, and two periodic ports were placed between the air regions and PMLs. The excitation port injected either an electric field \vec{E}_{\parallel} parallel to the C-resonator or an electric field \vec{E}_{\perp} perpendicular to it. Both the excitation and listener ports were set to pass the highest modes and diffraction modes of the metamaterial that were absorbed by the PMLs after passing. This allowed us to track the energy change in the initially excited waves and avoid setting many extra diffraction ports, which would increase the calculation time. In addition, these ports were far away enough, and we were able to exclude the capture of excited resonance modes. The Floquet cell was closed with perfect electric boundary conditions (PECs). Since the radiation absorbed by the PMLs passed through the ports, these boundary conditions had almost no effect.

For obtaining the transmitted spectra, we calculated the squared amplitude of the S-parameter S_{21} . Meanwhile, to retrieve the phase change $\Delta\varphi_{tr}$ induced by the metamaterial, we excluded from the argument of the parameter S_{21} the phase shift induced by the air medium with thickness $2 \cdot t_{air}$ and the substrate with thickness $t_s = 15 \mu\text{m}$:

$$\Delta\varphi_{tr} = \arg[S_{21}^* \cdot \exp(-i \cdot k \cdot [2 \cdot n_{air} \cdot t_{air}])] \quad (4)$$

4. Fabrication Process

4.1. Spiral Metamaterial Production

The standard contact photolithography technique was used for the fabrication of the spiral metamaterial on polypropylene (Figure 2a). The PP film was stretched over aluminum rings with an aperture diameter of 3 inches. Aluminum metallization was applied to polypropylene films by vacuum thermal deposition. A full description of every stage of the production can be found in [40]. Here we mention several drawbacks of the materials and production process, which can lead to experimental errors:

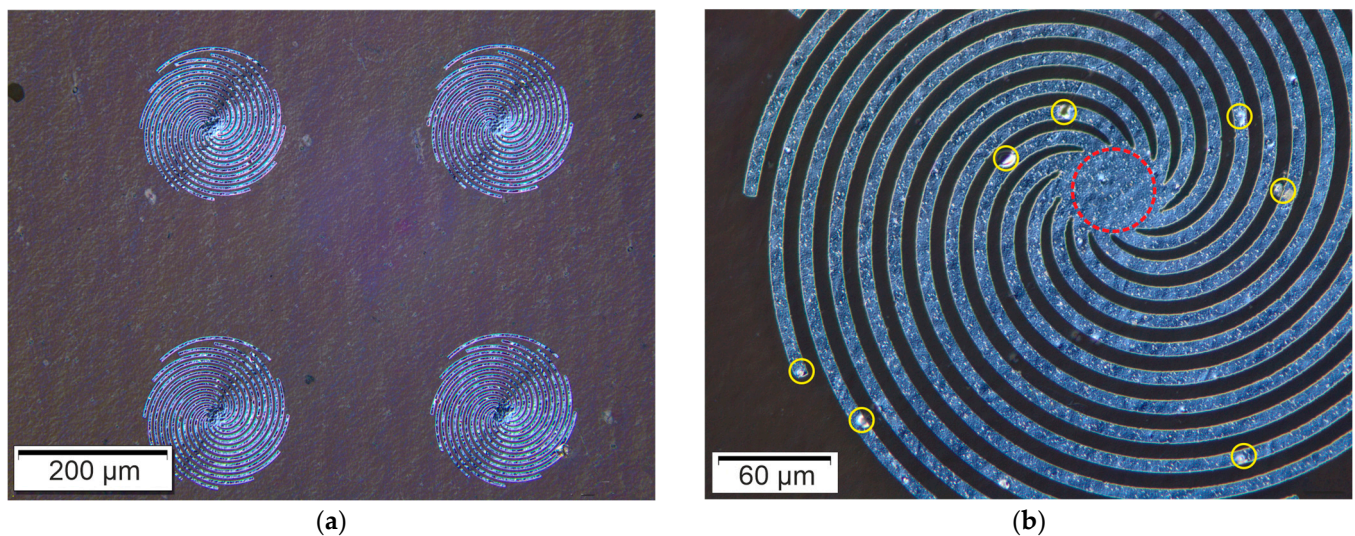


Figure 2. (a) Microscopy image of metamaterial and (b) detail image of the spiral structure and its defects.

Micro-bumps of granules, protruding above the surface of the polypropylene film, can lead to local delamination of the metallization, as can be seen in Figure 2b (yellow rings).

1. A circle with small ellipticity appears in the center of each spiral structure because of the limitation of the fabrication process (the red ring in Figure 2b).
2. Local tensions of the PP film may result in deviations in the topological dimensions.

4.2. Photoresist Deposition

To analyze the sensing capability of the structure to thin films, we used the photoresistive material (AR-P 3250, produced by ALLRESIST (GmbH, Strausberg, Germany) [41], of variable thickness t_a (1 μm to 10 μm) on the metastructure. It was applied by the standard spin coating technique.

We considered the thin layer of the photoresist as a nondispersive and loss-less analyte with $\varepsilon_a = 2.65$ ($n_a = 1.63$), which was evaluated in the THz spectral range from the results of time-domain spectroscopy measurements with thick photoresist layers [42]. However, in our measurements, the use of this material as a test analyte has some disadvantages. In particular, its dielectric permittivity changes with time, and as a consequence, (1) the photoresist material dries out and its absorption coefficient drops in the terahertz range; (2) the refractive index of a thick sample layer can differ from that of a thin layer of this material. All this may lead to fluctuations in the refractive index and discrepancies in the results of simulation and experiment.

5. Experimental Setup

A quasi-optical spectrometer with a tuned backward wave oscillator (BWO) developed at GPI RAS [43] was used for measuring the amplitude and phase spectra in the frequency range of 0.2–0.5 THz. The THz beam with a diameter of 26 mm was linearly polarized in a horizontal plane. During both the amplitude and phase measurements, the direction of polarization relative to the metamaterial was controlled via changes in the metasurface orientation. \vec{E}_{\parallel} corresponded to the C-resonator placed parallel to the polarization of the beam, whereas \vec{E}_{\perp} corresponded to its perpendicular position.

5.1. Amplitude Measurement

We measured the amplitude spectra of a wave transmitted through the optical system shown in Figure 3. The conical wavefront of a TM-polarized wave of the BWO was collimated by a polyethylene lens. After that, a diffraction-limited Gaussian beam radiated into the free space and passed through the obturator and the sample. By means of a mirror and a lens, it was directed to a Golay cell, which was used as a broadband THz detector in combination with a lock-in amplifier. The experimental parameter $|S_{21}|^2$ was defined as the ratio of the intensity I_{sample} of the beam transmitted through the sample to the intensity I_{free} of the beam passed through the experimental scheme without the sample:

$$|S_{21}|^2 = \frac{I_{sample}}{I_{free}} \tag{5}$$

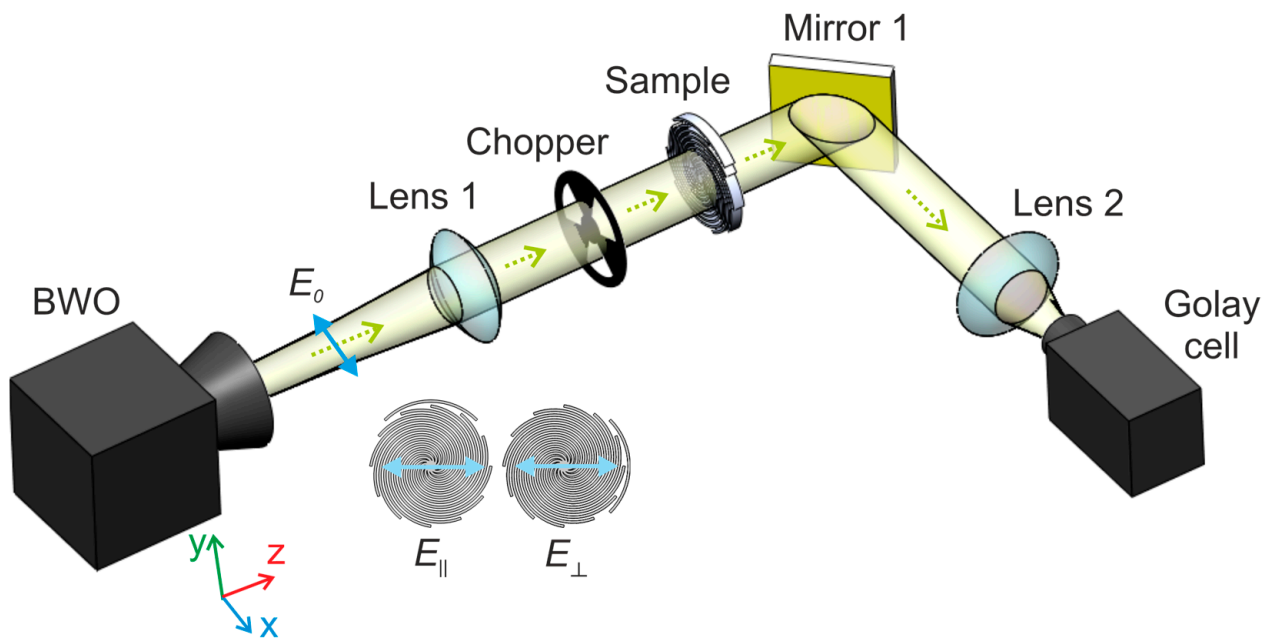


Figure 3. Scheme of the experimental setup for measuring amplitude spectra.

5.2. Phase Measurement

To measure the phase $\Delta\varphi_{tr}$ we set an additional interferometer arm using two beam splitters, as shown in Figure 4, and as a result, the Mach-Zander interferometer was formed. During the spectral measurements, the optical lengths of Arm II were tuned for maintaining a zero-order interference minimum. It was reached via a change in the position of mirror 2 with a motorized computer-controlled translator. The obturator was excluded from the setup and replaced by a speaker membrane attached to mirror 1, which periodically vibrated it. In this setup, calculation of $\Delta\varphi_{tr}$ was performed automatically with the software of the spectrometer registering the positions of mirror 2 X_{sample} and X_{free} in the variation of the setup with and without the sample, respectively:

$$\Delta\varphi_{tr} = \frac{2\pi}{\lambda} (X_{sample} - X_{free} + d) \tag{6}$$

where d is the thickness of the sample.

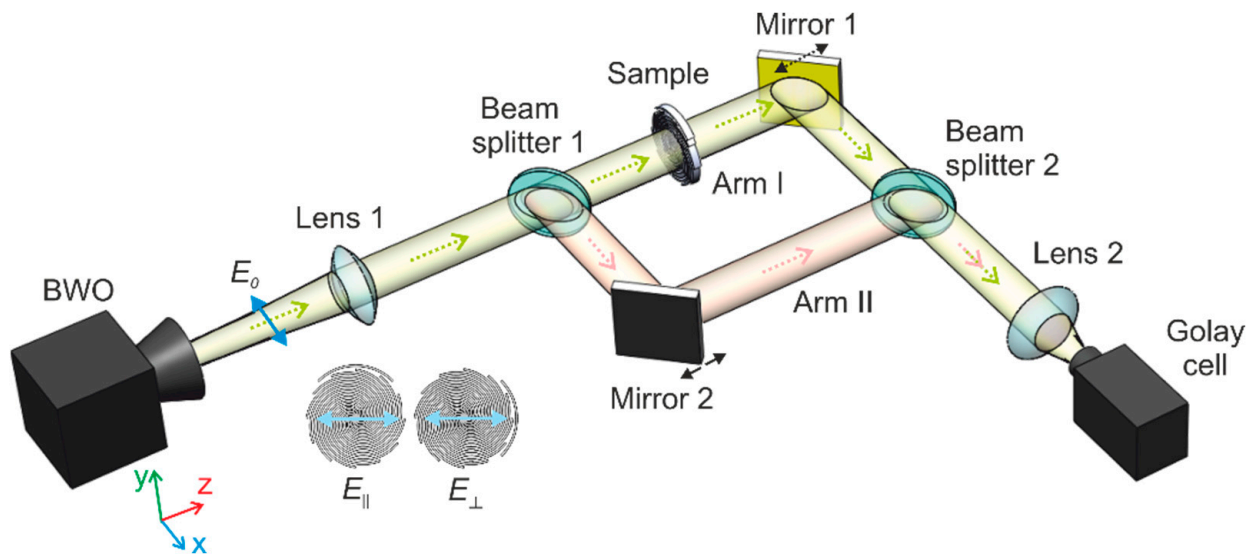


Figure 4. Scheme of the experimental setup for measuring phase spectra.

6. Results and Discussion

6.1. Comparison of the Simulation and Experimental Results

We first compared the amplitude, phase, and absolute gradient of the phase change spectra of the spiral metamaterial without analyte for the two polarization states obtained from the experiments and COMSOL simulations, as shown in Figure 5. The phase change was found via Equation (6), whereas the absolute gradient of the phase change was determined as $\Delta\phi'_{tr} = \left| \frac{d(\Delta\phi_{tr})}{df} \right|$. We excited four modes with a \vec{E}_{\parallel} -polarized wave due to the C-resonator (Figure 5a). The first mode (I) emerged at 0.297 THz and 0.302 THz in the experiments and the simulations, correspondingly. Since the same resonance was observed with a \vec{E}_{\perp} -polarized beam and was excited on the structure without a C-shaped resonator (Figure 5c), we can conclude that those were the fundamental modes. For the explanation of the following dip occurring at 0.34 THz (II), we calculated the phase and transmission spectra of a C-shaped resonator without a spiral disk, as can be seen in Figure 5a. The resonance position of this structure was close (0.343 THz) to the second dip. Thus, the resonance (II) comes from the LSP mode supported by the single C-shaped resonator, and it is a hybrid mode. The third dip emerged at 0.373 THz (III) and corresponded to the dark dipole mode. The narrowest resonances (IV) at 0.388 THz were the diffraction modes for both polarizations.

The main difference between the experiments and simulations is the absence of the well-defined diffraction mode and dark dipole mode at 0.373 THz in the experiment with the metamaterial without any coating. The primary reason is that in this measurement, these two dips merged with each other because of the diffraction mode broadening in the experiment due to the finite size and diffractive divergence of the incident beam. It should be noted that they became distinguishable (see Section 6.3) in the experimental spectra measured for the different analyte thicknesses due to different mode sensitivities. For this reason, the further analysis does not include experimental points of the diffraction mode obtained from the experiment.

Another distinction corresponds to the absolute amplitude dips. The experimental resonance dips were deeper than the simulated ones, which are associated with the increase in the absorption losses caused by the structural imperfections in the fabricated metasurfaces and diffraction effects. Moreover, there was a deviation between the resonance frequencies of the fundamental dipole mode in the experiment and the simulation. The simulated dipole mode was excited at 0.297 THz, while the experimental one emerged at 0.302 THz. The resonance frequency of the spiral structure strongly depends on its parameters (for

instance, see Equation (2)). This discrepancy is due to parameter fluctuations caused by manufacturing inaccuracies (see Section 4).

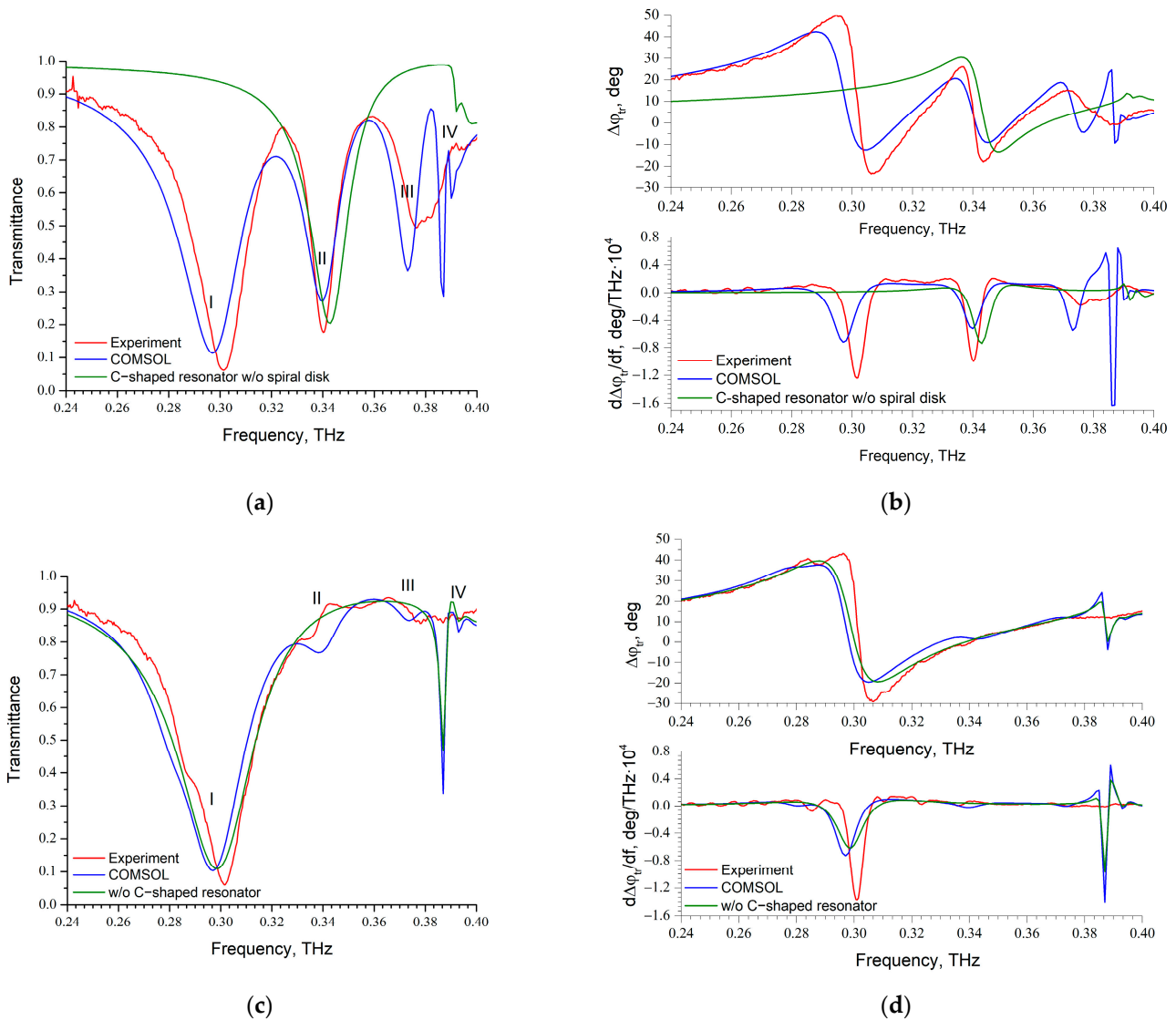


Figure 5. Amplitude (left) and phase (right) spectra: (a,b) \vec{E}_{\parallel} , (c,d) \vec{E}_{\perp} .

Finally, because the dips of the fundamental and diffraction modes are identical for both polarization states, we only analyzed the spectra corresponding to \vec{E}_{\parallel} . Moreover, the phase spectra do not enable improvements in the sensor performance, and for this reason, we studied only the gradient of the phase change spectra.

6.2. Simulation Results: Resonant Mechanism of Metamaterial

The vertical electric fields of the metamaterial were collected at the resonant dip frequencies for illustration of the resonant physical mechanism in resonant modes excited by \vec{E}_{\parallel} . The distributions of the electric field E_z are shown in Figure 6. The low-frequency resonance mode (Figure 6a) at $f_1 = 0.297$ THz corresponds to the fundamental mode that can be excited without any C-resonator. The minimum and maximum of the electric field concentrate on the different sides of the spiral structure, forming the electric dipole resonance. Adding C-resonator enables the excitation of additional modes. Figure 6b,c depict the electric fields of the metamaterial structure at two resonant frequencies ($f_2 = 0.34$ THz and $f_3 = 0.373$ THz), which maxima vary along the radial direction. Thus, we can conclude

that these two resonances are magnetic dipole resonances. Besides, the resonance f_2 is very close to the fundamental mode of the C-resonator, which correspond to hybridized nature of f_2 . The position of the fourth resonance is determined via Equation (3), which is the diffraction resonance mode at $f_4 = 0.388$ THz.

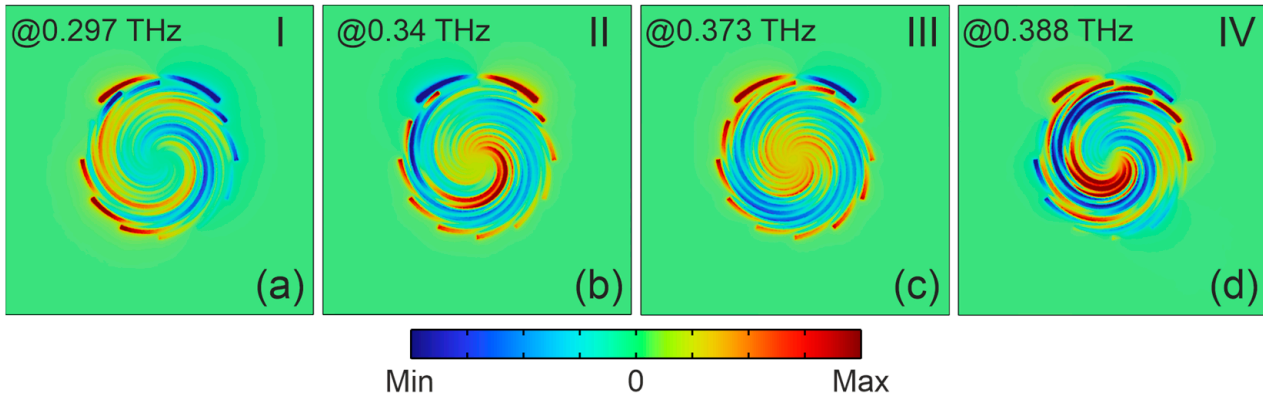


Figure 6. Simulated near field patterns of vertical electric field (E_z) of (a) fundamental dipole resonance mode at $f_1 = 0.297$ THz, (b) hybrid dipole resonance mode at $f_2 = 0.34$ THz, (c) dark dipole resonance mode at $f_3 = 0.373$ THz, and (d) diffraction mode at $f_4 = 0.388$ THz on transverse x - y plane $10 \mu\text{m}$ above the upper metallic spiral surface.

6.3. Sensing Performance

The terahertz metamaterial can be used as a sensor for substance detection. The analytes covering the surface of the metamaterial lead to a change in the ambient dielectric permittivity, which in turn results in the shift of the resonant frequency of the THz transmission spectrum of the metamaterial. It is possible to estimate the refractive indices of the analytes via measurement of the offset of the resonance dips and distinguish different substances. In addition, if the parameters of samples are known, the metamaterial can be used for thickness measurement based on the fact that the frequency offset depends on the thickness. To quantify the performance of the sensors we conducted experiments and simulations with the proposed metamaterial coated with dielectric layers; the results are shown in Figure 7.

To obtain further insight into the resonances capabilities of the spiral structure, we defined the frequency shift as $\Delta f = \frac{f_{ref} - f_{ta}}{f_{ref}} \cdot 100\%$, where f_{ta} is the resonance frequency of the spiral metamaterial coated with an analyte with thickness t_a , and f_{ref} is the resonance frequency of the metamaterial without any analyte coating. We plotted the measured and simulated frequency shifts of the spiral metamaterials in Figure 8. The fitting function can be described as $\Delta f = \Delta f_s \left(1 - \exp\left(-\frac{t_a}{t_s}\right) \right)$, where Δf_s is the saturation frequency shift and t_s is the saturation thickness of the sensor. We fitted the simulation and experimental results, and the good match of this approximation with the data indicates that the boundary fields exponentially decayed from the top surface of the sensor. Meanwhile, the experimental data show a systematic deviation from the simulation results. This is due to the fluctuations in the refractive index of the analyte over time, as was described in Section 4.

In general, three main parameters enable the evaluation of the sensing performance of the metamaterials: refractive index sensitivity (S), Q factor (Q), and figure of merit (FOM). The sensitivity reflects the relationship between the resonant frequency shift df induced by the addition of analytes and the change in the refractive index dn , that is, $S = df/dn$. Because we have analytes with similar refractive indices, but different thicknesses, we can formally estimate the sensitivity by assuming that the resonance frequency shift is in a linear dependence on the refractive index $f_{res} = f_{ref} + S \cdot (n_a - n_{ref})$, where $n_{ref} = n_{air} = 1$ is the refractive index of the media surrounding the bare metamaterial. Thus, taking into account the influence of the analyte thickness on the sensitivity, we obtain $S = \frac{\Delta f}{n_a - n_{ref}}$.

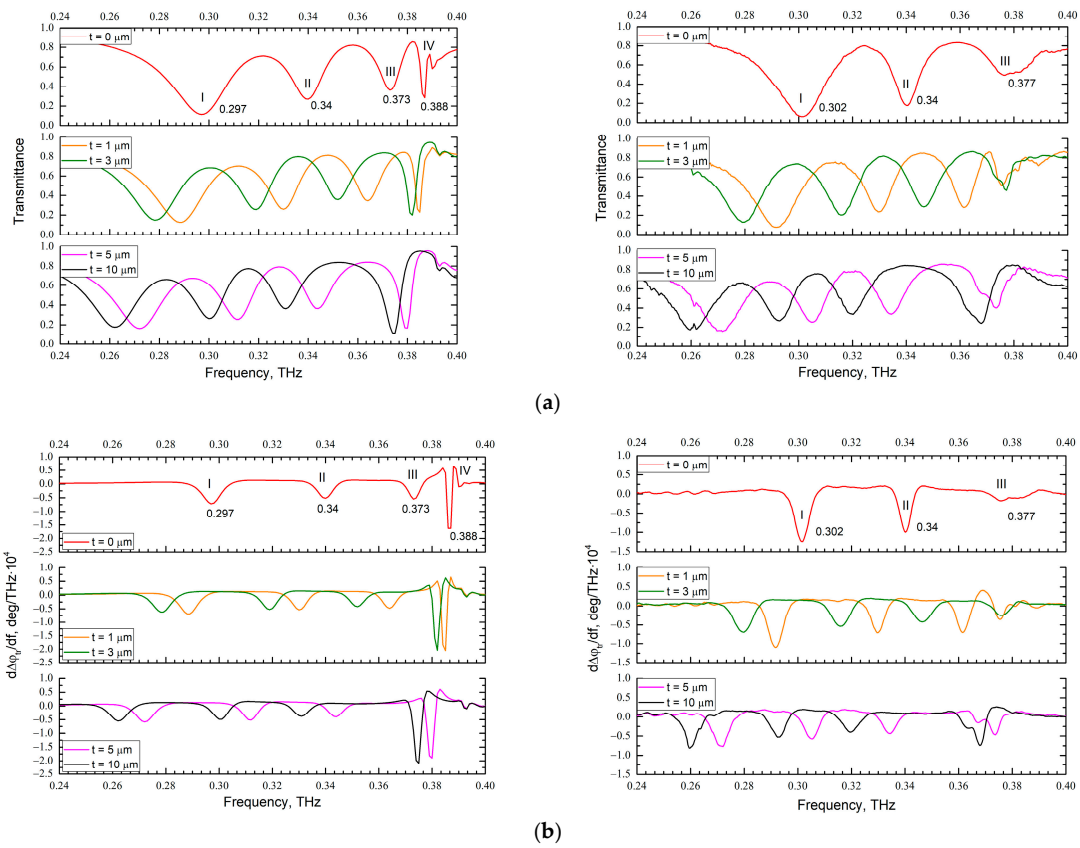


Figure 7. Simulation (left) and experimental (right) spectra: (a) amplitude, (b) phase.

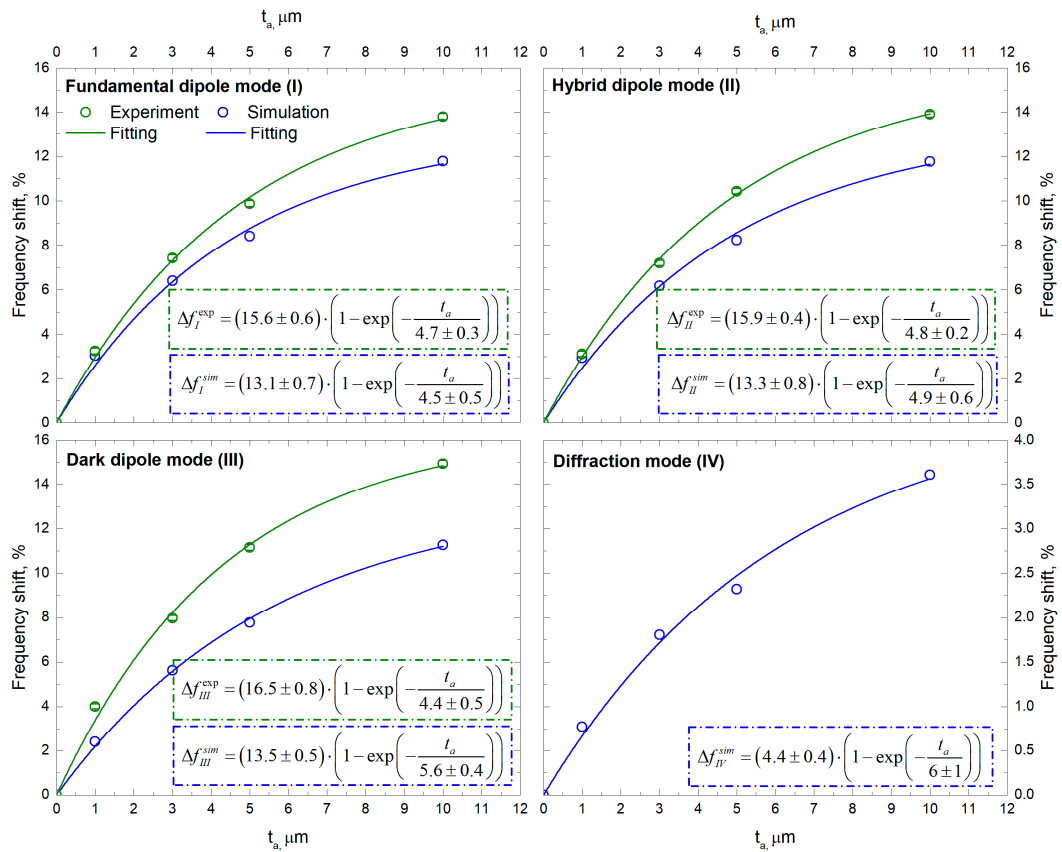


Figure 8. Frequency shift versus analyte thickness.

As shown in Figure 9, as the thickness of the analyte layer increased, the refractive index sensitivity of the sensor significantly grew. The sensitivity went up with the factor $e = 2.72$ with the layer thickness t_s , which corresponds to 63% of the maximum sensitivity S_{\max} . From the point of sensing applications, we assumed that the optimal thickness was $t_a \geq 2 \cdot t_s$ ($\geq 87\%$ of S_{\max}), because after that no increase in the refractive index sensitivity was evident anymore. The analyte thickness was beyond the range of the distance that the electromagnetic field affects, which alternatively influences the sensing performance of the sensor. The maximum sensitivity can be determined as $S_{\max} = \frac{\Delta f_s}{n_a - n_{ref}}$.

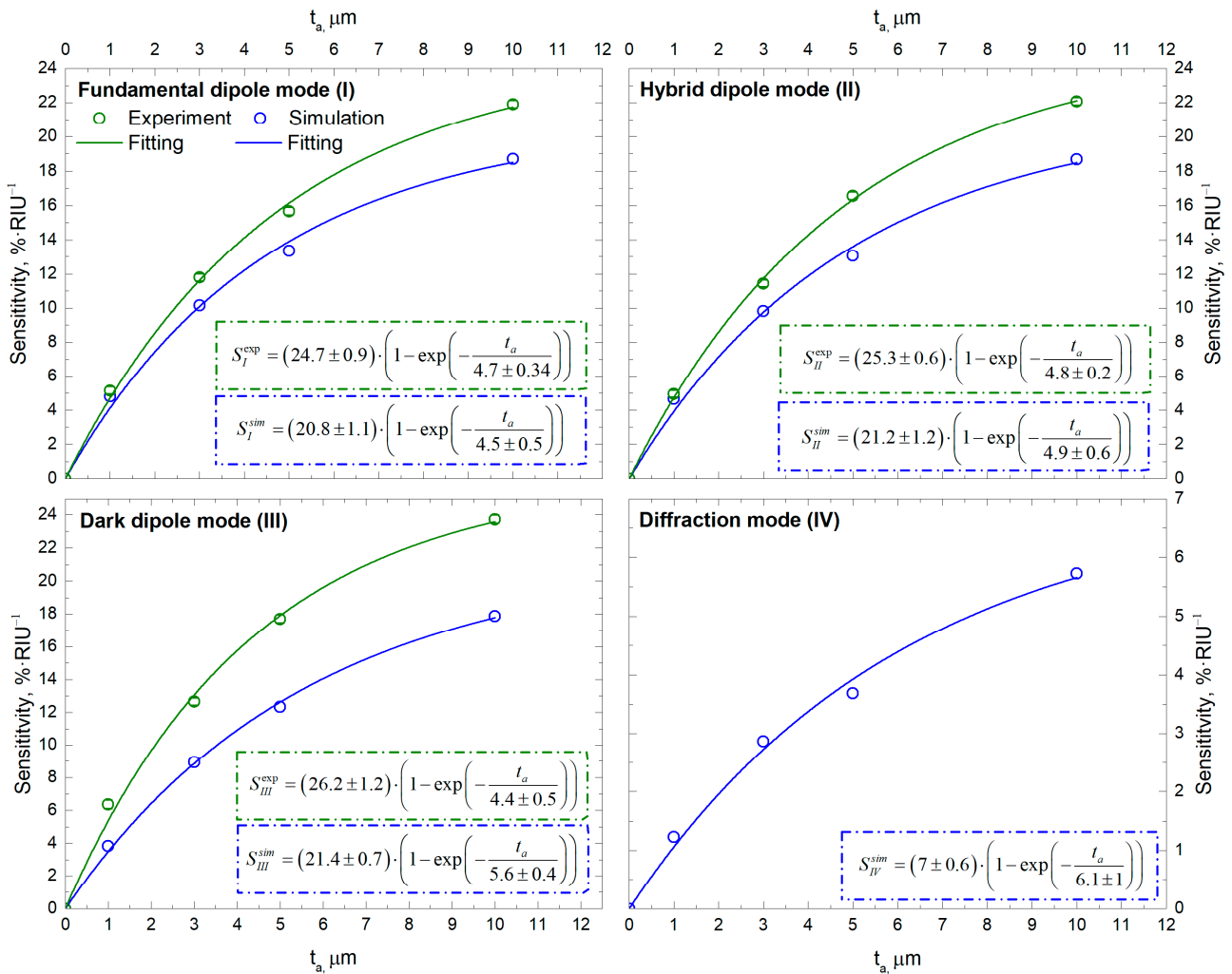


Figure 9. Sensitivity versus analyte thickness.

The fundamental and dark resonance modes are dipole modes, but they work at different frequencies; within the observational error, they have the same sensitivities. We estimated the sensitivities of the dipole modes as $S_{\max}^{\text{sim}} = 21.1 \pm 1\%/\text{RIU}$ for the modeling results. As was mentioned earlier, the refractive index of the analyte differed from the simulated value. It is possible to estimate the experimental refractive index of the analyte based on the measurements. Assuming that $\Delta f_{\text{exp}}/S_{\max}^{\text{sim}} + n_{\text{ref}} = n_a$, we obtain $(15.6 \pm 0.6)/(21.1 \pm 1) + 1 = 1.74 \pm 0.15$, and then the experimental sensitivity is $S_{\max}^{\text{exp}} = 22.3 \pm 3\%/\text{RIU}$.

The next parameter of the sensor is the quality factor $Q = \frac{f_{\text{res}}}{FWHM}$, where $FWHM$ is the full width at half-minimum of the resonant dip. The higher the Q factor (the narrower is $FWHM$), the easier is it to distinguish the offset of the resonant dip. The quality factor changed slightly with a variation in the analyte thickness (see Figure 10).

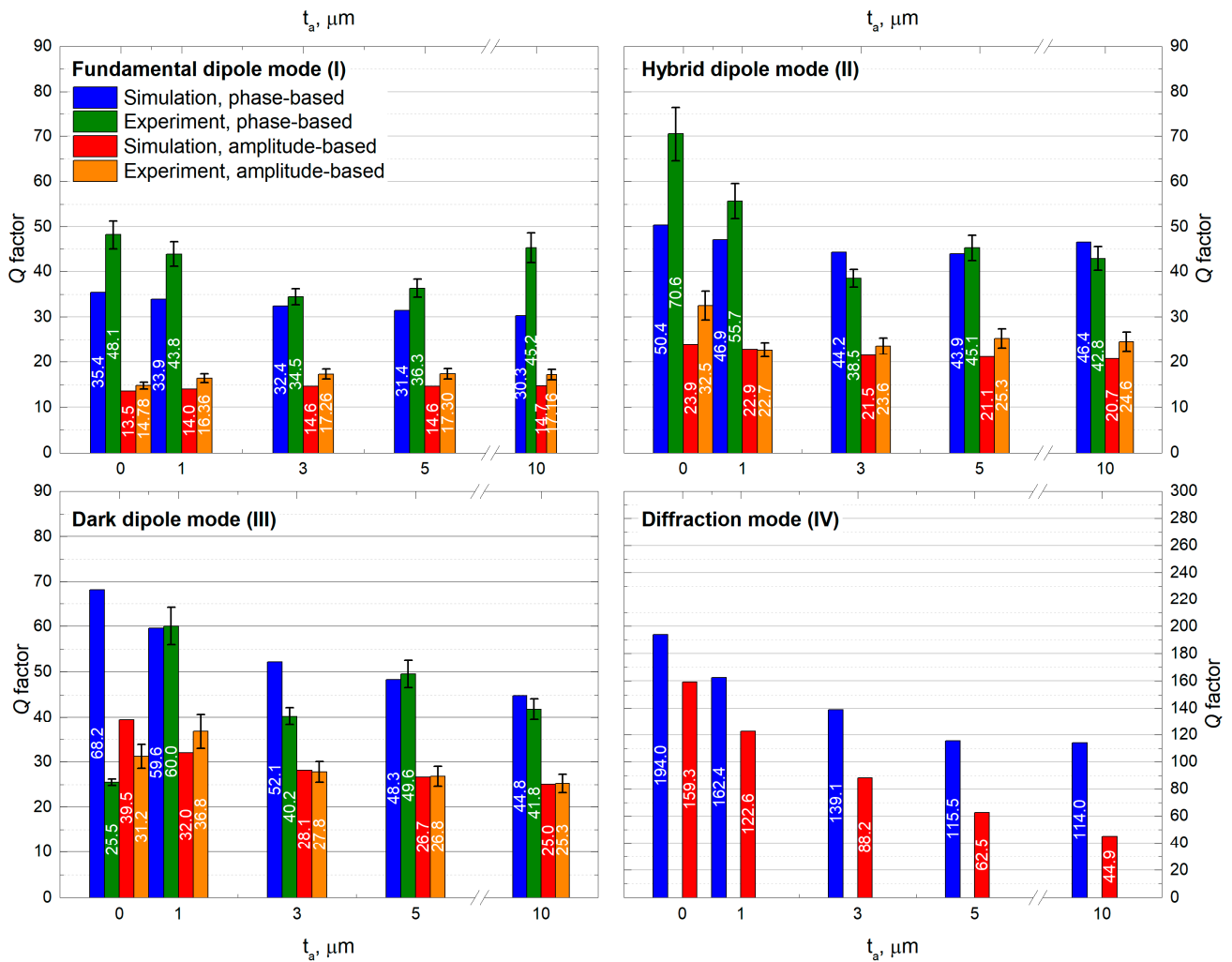


Figure 10. Q factor versus analyte thickness.

In the amplitude measurements, the best Q factor was observed for the dipole modes excited with the C-shaped resonator; it was $Q_{II}^{sim} = 39.5$ for the modeling and $Q_{II}^{exp} = 32.5 \pm 3.2$ for the experimental results, whereas for the fundamental dipole mode, it was $Q_I^{sim} = 13.5$ and $Q_I^{exp} = 14.8 \pm 0.8$, correspondingly. The Q factor of the hybrid dipole mode at 0.34 THz was better in the experiment because it was clearly distinguishable. In terms of this parameter, the dark dipole mode is almost three times better than the fundamental mode. To compare the quality factor obtained from the phase measurement, almost twice the best quality factor is shown. So, the results were $Q_{III}^{sim} = 68.2$, $Q_{III}^{exp} = 70.6 \pm 6$, $Q_I^{sim} = 35.4$, and $Q_I^{exp} = 48.1 \pm 3.2$. Increasing the quality factor is the main reason for using phase measurements for dark dipole modes in sensor applications.

For a further quantitative description of the proposed sensor, we calculated the figure of merit (FOM), which is regularly used for comparison of the sensing performance of the sensor in different frequency bands. Higher FOM values correspond to better sensing performance. We defined the FOM as $FOM = \frac{S \cdot f_{ref}}{FWHM \cdot 100\%} = \frac{S \cdot Q_{ref}}{100\%}$, where Q_{ref} is the quality factor of the resonance of the bare metamaterial. The results are demonstrated in Figure 11. The FOM goes up with increasing analyte thickness because this parameter is inversely proportional to the sensitivity. We can estimate the maximum FOM as $FOM = \frac{S_{max} \cdot Q_{ref}}{100\%}$. For the amplitude and phase measurements, they were $FOM_{max}^{sim} = 8.3 \pm 0.4 \text{ RIU}^{-1}$ and $FOM_{max}^{sim} = 14.4 \pm 0.7 \text{ RIU}^{-1}$ correspondingly.

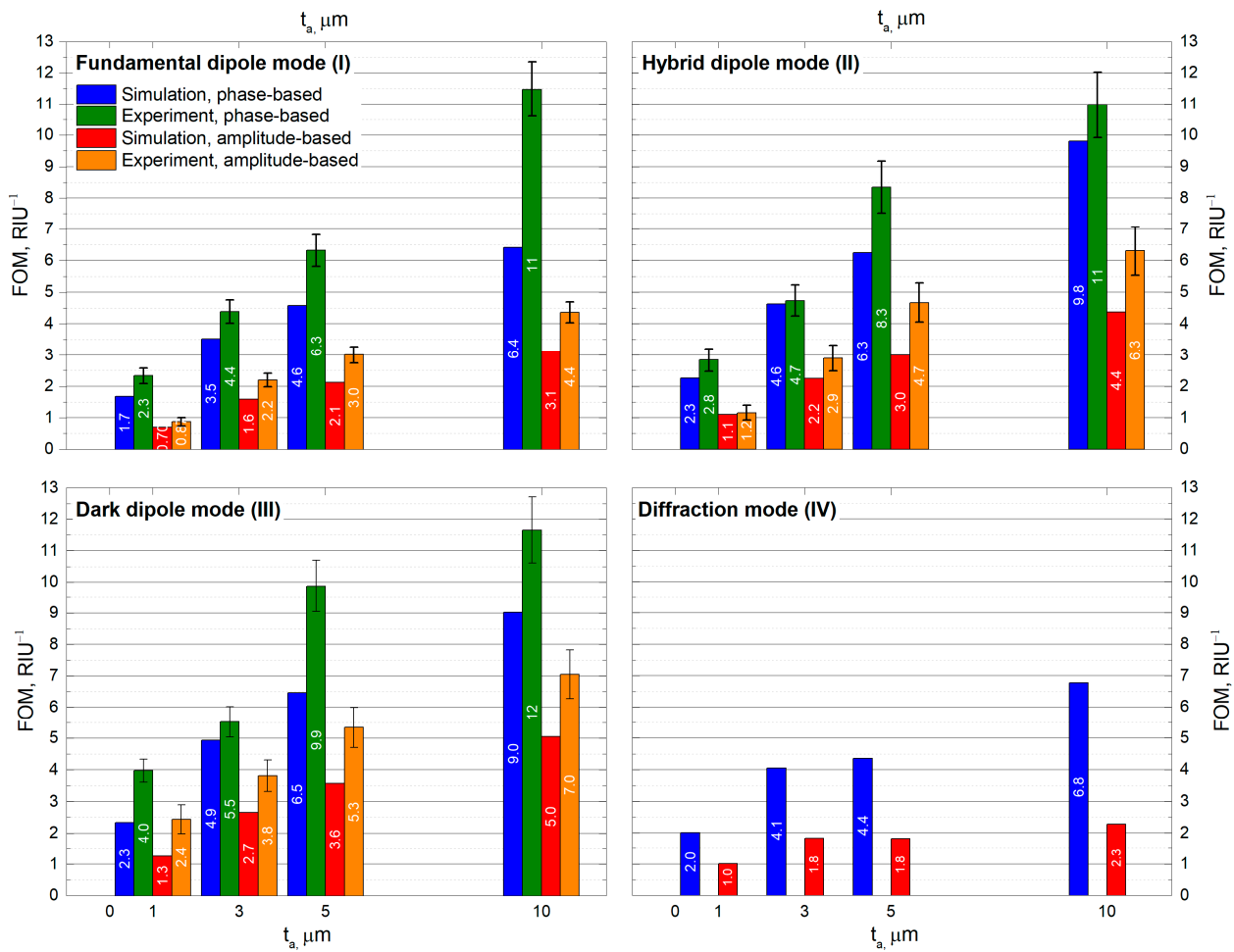


Figure 11. FOM versus analyte thickness.

As can be seen in Table 1, the sensing performance of the proposed sensor is comparable to or better than those recently reported in the literature. It could be concluded that the spiral metamaterial provides one of the highest FOMs and Q factors among analogs. Moreover, due to its several resonance modes, it can characterize identical samples at multiple frequencies, thereby increasing the selectivity and sensitivity of detection.

Table 1. Comparison of the sensing performance of the proposed sensor with previously reported analogs.

f _{ref} , THz	S, %/RIU	Q _{ref}		FOM, RIU ⁻¹		Ref.
		amp	Phase	amp	Phase	
0.373	21.1	39.5	68.2	8.3	14.4	This work
2.88	31.7	7.87	-	2.49	-	[44]
0.97	31.3	7.65	-	2.47	-	[45]
1.71	31.6	9.2	-	2.86	-	[46]
0.68	23.7	11.6	-	2.3	-	[47]
0.81	23.5	11	-	1.98	-	[48]
1.04	29.7	9.96	-	2.97	-	[49]
2.95	24.8	10.17	-	2.52	-	[50]
0.21	-	30	-	-	-	[51]
0.738	50.1	10.5	43.4	5.3	21.7	[14]

7. Conclusions

To conclude, we have demonstrated an Archimedean spiral metamaterial with a C-shaped resonator as a sensor in the THz regime and compared thin film sensing potentials of the fundamental and dark resonant modes. The comprehensive study has been conducted with an oft-neglected source of information in the field of sensing: the phase of electromagnetic fields. It has been observed that the dark dipole mode had a FOM and a Q factor almost three times as high as those of the fundamental resonance mode. We have shown that the phase-based FOM and Q factor are about twice as high as those of its amplitude-based counterpart, which makes the phase response capability of higher resolution in spectral characterization. A sensitivity of 21.1%/RIU (78.7 GHz/RIU) and a FOM of 14.4 RIU⁻¹ have been achieved. The design of the metamaterial is a highly flexible platform for THz sensing, and these characteristics can be improved through its modifications in further investigations. More importantly, the phase as an output response is expected to provide new opportunities for high-performance refractive index sensing and thickness measurement.

Author Contributions: This work was realized through the collaboration of all authors. O.K.: contributing to the main results, writing—original draft preparation; V.G.: reviewing and editing, experimental investigation, funding acquisition; S.K.: editing, sample preparation, scientific discussion. All authors have read and agreed to the published version of the manuscript.

Funding: The work was partially supported by the Ministry of Science and Higher Education of the Russian Federation, grant FSUS-2020-0029.

Acknowledgments: The work was fulfilled at the shared research center SSTRC based on the Novosibirsk FEL at BINP SB RAS and the Shared Equipment Center CKP “VTAN” (ATRC) of the NSU Physics Department.

Conflicts of Interest: The authors declare no conflict of interest.

References

1. Maier, S.A. *Others Plasmonics: Fundamentals and Applications*; Springer: Berlin/Heidelberg, Germany, 2007; Volume 1.
2. Willets, K.A.; Wilson, A.J.; Sundaresan, V.; Joshi, P.B. Super-Resolution Imaging and Plasmonics. *Chem. Rev.* **2017**, *117*, 7538–7582. [[CrossRef](#)] [[PubMed](#)]
3. Fang, Y.; Sun, M. Nanoplasmonic Waveguides: Towards Applications in Integrated Nanophotonic Circuits. *Light Sci. Appl.* **2015**, *4*, e294. [[CrossRef](#)]
4. Olaimat, M.M.; Yousefi, L.; Ramahi, O.M. Using Plasmonics and Nanoparticles to Enhance the Efficiency of Solar Cells: Review of Latest Technologies. *J. Opt. Soc. Am. B* **2021**, *38*, 638. [[CrossRef](#)]
5. Ge, W.; Zhang, X.R.; Liu, M.; Lei, Z.W.; Knize, R.J.; Lu, Y. Distance Dependence of Gold-Enhanced Upconversion Luminescence in Au/SiO₂/Y₂O₃: Yb³⁺, Er³⁺ + Nanoparticles. *Theranostics* **2013**, *3*, 282–288. [[CrossRef](#)] [[PubMed](#)]
6. Zhang, X.; Xu, Q.; Xia, L.; Li, Y.; Gu, J.; Tian, Z.; Ouyang, C.; Han, J.; Zhang, W. Terahertz Surface Plasmonic Waves: A Review. *Adv. Photon.* **2020**, *2*, 1. [[CrossRef](#)]
7. Shelby, R.A.; Smith, D.R.; Schultz, S. Experimental Verification of a Negative Index of Refraction. *Science* **2001**, *292*, 77–79. [[CrossRef](#)]
8. Schurig, D.; Mock, J.J.; Justice, B.J.; Cummer, S.A.; Pendry, J.B.; Starr, A.F.; Smith, D.R. Metamaterial Electromagnetic Cloak at Microwave Frequencies. *Science* **2006**, *314*, 977–980. [[CrossRef](#)] [[PubMed](#)]
9. Cai, W.; Chettiar, U.K.; Kildishev, A.V.; Shalaev, V.M. Optical Cloaking with Metamaterials. *Nat. Photon* **2007**, *1*, 224–227. [[CrossRef](#)]
10. Pendry, J.B.; Martín-Moreno, L.; Garcia-Vidal, F.J. Mimicking Surface Plasmons with Structured Surfaces. *Science* **2004**, *305*, 847–848. [[CrossRef](#)]
11. Garcia-Vidal, F.J.; Fernández-Domínguez, A.I.; Martín-Moreno, L.; Zhang, H.C.; Tang, W.; Peng, R.; Cui, T.J. Spoof Surface Plasmon Photonics. *Rev. Mod. Phys.* **2022**, *94*, 025004. [[CrossRef](#)]
12. Rusina, A.; Durach, M.; Stockman, M.I. Theory of Spoof Plasmons in Real Metals. *Appl. Phys. A* **2010**, *100*, 375–378. [[CrossRef](#)]
13. Ng, B.; Wu, J.; Hanham, S.M.; Fernández-Domínguez, A.I.; Klein, N.; Liew, Y.F.; Breese, M.B.H.; Hong, M.; Maier, S.A. Spoof Plasmon Surfaces: A Novel Platform for THz Sensing. *Adv. Opt. Mater.* **2013**, *1*, 543–548. [[CrossRef](#)]
14. Huang, Y.; Zhong, S.; Shi, T.; Shen, Y.; Cui, D. Terahertz Plasmonic Phase-Jump Manipulator for Liquid Sensing. *Nanophotonics* **2020**, *9*, 3011–3021. [[CrossRef](#)]
15. Yao, H.; Zhang, W.; Liu, W.; Mei, H. Resolved Terahertz Spectroscopy of Tiny Molecules Employing Tunable Spoof Plasmons in an Otto Prism Configuration. *J. Opt.* **2022**, *24*, 045301. [[CrossRef](#)]

16. Shen, X.; Jun Cui, T. Planar Plasmonic Metamaterial on a Thin Film with Nearly Zero Thickness. *Appl. Phys. Lett.* **2013**, *102*, 211909. [CrossRef]
17. Pors, A.; Moreno, E.; Martin-Moreno, L.; Pendry, J.B.; Garcia-Vidal, F.J. Localized Spoof Plasmons Arise While Texturing Closed Surfaces. *Phys. Rev. Lett.* **2012**, *108*, 223905. [CrossRef]
18. Gao, Z.; Wu, L.; Gao, F.; Luo, Y.; Zhang, B. Spoof Plasmonics: From Metamaterial Concept to Topological Description. *Adv. Mater.* **2018**, *30*, 1706683. [CrossRef]
19. Zhang, X.; Cui, W.Y.; Lei, Y.; Zheng, X.; Zhang, J.; Cui, T.J. Spoof Localized Surface Plasmons for Sensing Applications. *Adv. Mater. Technol.* **2021**, *6*, 2000863. [CrossRef]
20. Chen, L.; Wei, Y.; Zang, X.; Zhu, Y.; Zhuang, S. Excitation of Dark Multipolar Plasmonic Resonances at Terahertz Frequencies. *Sci. Rep.* **2016**, *6*, 22027. [CrossRef]
21. Shao, R.L.; Zhou, Y.J.; Yang, L. Quarter-Mode Spoof Plasmonic Resonator for a Microfluidic Chemical Sensor. *Appl. Opt.* **2018**, *57*, 8472. [CrossRef]
22. Zhou, J.; Chen, L.; Sun, Q.; Liao, D.; Ding, L.; Balakin, A.V.; Shkurinov, A.P.; Xie, J.; Zang, X.; Cheng, Q.; et al. Terahertz On-Chip Sensing by Exciting Higher Radial Order Spoof Localized Surface Plasmons. *Appl. Phys. Express* **2020**, *13*, 012014. [CrossRef]
23. Huidobro, P.A.; Shen, X.; Cuerda, J.; Moreno, E.; Martin-Moreno, L.; Garcia-Vidal, F.J.; Cui, T.J.; Pendry, J.B. Magnetic Localized Surface Plasmons. *Phys. Rev. X* **2014**, *4*, 021003. [CrossRef]
24. Liao, Z.; Shen, X.; Pan, B.C.; Zhao, J.; Luo, Y.; Cui, T.J. Combined System for Efficient Excitation and Capture of LSP Resonances and Flexible Control of SPP Transmissions. *ACS Photonics* **2015**, *2*, 738–743. [CrossRef]
25. Gao, Z.; Gao, F.; Zhang, Y.; Zhang, B. Deep-Subwavelength Magnetic-Coupling-Dominant Interaction among Magnetic Localized Surface Plasmons. *Phys. Rev. B* **2016**, *93*, 195410. [CrossRef]
26. Gao, Z.; Gao, F.; Zhang, B. High-Order Spoof Localized Surface Plasmons Supported on a Complementary Metallic Spiral Structure. *Sci. Rep.* **2016**, *6*, 24447. [CrossRef]
27. Liao, Z.; Fernández-Domínguez, A.I.; Zhang, J.; Maier, S.A.; Cui, T.J.; Luo, Y. Homogenous Metamaterial Description of Localized Spoof Plasmons in Spiral Geometries. *ACS Photonics* **2016**, *3*, 1768–1775. [CrossRef]
28. Liao, Z.; Liu, S.; Ma, H.F.; Li, C.; Jin, B.; Cui, T.J. Electromagnetically Induced Transparency Metamaterial Based on Spoof Localized Surface Plasmons at Terahertz Frequencies. *Sci. Rep.* **2016**, *6*, 27596. [CrossRef]
29. Zhang, J.; Liao, Z.; Luo, Y.; Shen, X.; Maier, S.A.; Cui, T.J. Spoof Plasmon Hybridization: Spoof Plasmon Hybridization. *Laser Photonics Rev.* **2017**, *11*, 1600191. [CrossRef]
30. Huang, Y.; Zhang, J.; Cui, T.J.; Liao, Z.; Zhang, D.H. Revealing the Physical Mechanisms behind Large Field Enhancement in Hybrid Spoof Plasmonic Systems. *J. Opt. Soc. Am. B* **2018**, *35*, 396. [CrossRef]
31. Su, H.; Shen, X.; Su, G.; Li, L.; Ding, J.; Liu, F.; Zhan, P.; Liu, Y.; Wang, Z. Efficient Generation of Microwave Plasmonic Vortices via a Single Deep-Subwavelength Meta-Particle. *Laser Photonics Rev.* **2018**, *12*, 1800010. [CrossRef]
32. Wang, Z.; Gao, Z.; Zhang, Y.; An, P.; Lou, J.; Cheng, P.; Zhao, H. Selectively Enhanced Magnetic Vertical Conductive Coupling among Magnetic Localized Surface Plasmons. *J. Phys. D Appl. Phys.* **2019**, *52*, 135101. [CrossRef]
33. Gerasimov, V.V.; Hafizov, R.R.; Kuznetsov, S.A.; Lazorskiy, P.A. Exploiting Localized Surface Plasmon Resonances in Subwavelength Spiral Disks for THz Thin Film Sensing. *Appl. Sci.* **2020**, *10*, 3595. [CrossRef]
34. O'Hara, J.F.; Withayachumnankul, W.; Al-Naib, I. A Review on Thin-Film Sensing with Terahertz Waves. *J. Infrared Milli Terahz Waves* **2012**, *33*, 245–291. [CrossRef]
35. Akter, N.; Hasan, M.; Pala, N. A Review of THz Technologies for Rapid Sensing and Detection of Viruses Including SARS-CoV-2. *Biosensors* **2021**, *11*, 349. [CrossRef] [PubMed]
36. How to Build a Parameterized Archimedean Spiral Geometry. COMSOL Blog. Available online: <https://www.comsol.com/blogs/how-to-build-a-parameterized-archimedean-spiral-geometry> (accessed on 22 February 2023).
37. Kuznetsov, S.A.; Paulish, A.G.; Navarro-Cía, M.; Arzhannikov, A.V. Selective Pyroelectric Detection of Millimetre Waves Using Ultra-Thin Metasurface Absorbers. *Sci. Rep.* **2016**, *6*, 21079. [CrossRef]
38. Navarro-Cia, M.; Kuznetsov, S.A.; Aznabet, M.; Beruete, M.; Falcone, F.; Ayza, M.S. Route for Bulk Millimeter Wave and Terahertz Metamaterial Design. *IEEE J. Quantum Electron.* **2011**, *47*, 375–385. [CrossRef]
39. Sommerfeld, A. *Optics*; Academic Press: Cambridge, MA, USA, 1964; Volume 4.
40. Aznabet, M.; Navarro-Cia, M.; Kuznetsov, S.A.; Gelfand, A.V.; Fedorinina, N.I.; Goncharov, Y.G.; Beruete, M.; El Mrabet, O.; Sorolla, M. Polypropylene-Substrate-Based SRR- and CSRR- Metasurfaces for Submillimeter Waves. *Opt. Express* **2008**, *16*, 18312. [CrossRef]
41. ALLRESIST GmbH. Available online: <https://www.allresist.com> (accessed on 21 May 2020).
42. Jáuregui-López, I.; Rodríguez-Ulbarri, P.; Kuznetsov, S.; Nikolaev, N.; Beruete, M. THz Sensing With Anomalous Extraordinary Optical Transmission Hole Arrays. *Sensors* **2018**, *18*, 3848. [CrossRef]
43. Kozlov, G.; Volkov, A. Coherent Source Submillimeter Wave Spectroscopy. In *Millimeter and Submillimeter Wave Spectroscopy of Solids*; Grüner, G., Ed.; Topics in Applied Physics; Springer: Berlin/Heidelberg, Germany, 1998; Volume 74, pp. 51–109. ISBN 978-3-540-62860-6.
44. Lu, X.; Ge, H.; Jiang, Y.; Zhang, Y. A Dual-Band High-Sensitivity THz Metamaterial Sensor Based on Split Metal Stacking Ring. *Biosensors* **2022**, *12*, 471. [CrossRef]

45. Keshavarz, A.; Vafapour, Z. Sensing Avian Influenza Viruses Using Terahertz Metamaterial Reflector. *IEEE Sens. J.* **2019**, *19*, 5161–5166. [[CrossRef](#)]
46. Cong, L.; Tan, S.; Yahiaoui, R.; Yan, F.; Zhang, W.; Singh, R. Experimental Demonstration of Ultrasensitive Sensing with Terahertz Metamaterial Absorbers: A Comparison with the Metasurfaces. *Appl. Phys. Lett.* **2015**, *106*, 031107. [[CrossRef](#)]
47. Lu, X.; Ge, H.; Jiang, Y.; Zhang, Y. Design and Analysis of a Dual-Band THz Metamaterial Sensor with High Refractive Index Sensitivity. *Front. Phys.* **2022**, *10*, 973033. [[CrossRef](#)]
48. Ahmadivand, A.; Gerislioglu, B.; Tomitaka, A.; Manickam, P.; Kaushik, A.; Bhansali, S.; Nair, M.; Pala, N. Extreme Sensitive Metasensor for Targeted Biomarkers Identification Using Colloidal Nanoparticles-Integrated Plasmonic Unit Cells. *Biomed. Opt. Express* **2018**, *9*, 373. [[CrossRef](#)] [[PubMed](#)]

Disclaimer/Publisher's Note: The statements, opinions and data contained in all publications are solely those of the individual author(s) and contributor(s) and not of MDPI and/or the editor(s). MDPI and/or the editor(s) disclaim responsibility for any injury to people or property resulting from any ideas, methods, instructions or products referred to in the content.